The Astrophysical Journal, 972:159 (15pp), 2024 September 10 https://doi.org/10.3847/1538-4357/ad5ffb

Are WASP-107-like Systems Consistent with High-eccentricity Migration?

Hang Yu[1] and Fei Dai[2]
[1] eXtreme Gravity Institute, Department of Physics, Montana State University, Bozeman, MT 59717, USA; hang.yu2@montana.edu
[2] Institute for Astronomy, University of Hawai'i, 2680 Woodlawn Drive, Honolulu, HI 96822, USA; fdai@hawaii.edu
Received 2024 May 21; revised 2024 July 4; accepted 2024 July 6; published 2024 September 4

Abstract

WASP-107 b seems to be a poster child of the long-suspected high-eccentricity migration scenario. It is on a 5.7 day, polar orbit. The planet is Jupiter-like in radius but Neptune-like in mass with exceptionally low density. WASP-107 c is on a 1100 day, $e = 0.28$ orbit with at least Saturn mass. Planet b may still have a residual eccentricity of 0.06 ± 0.04: the ongoing tidal dissipation leads to the observed internally heated atmosphere and hydrodynamic atmospheric erosion. We present a population synthesis study coupling octupole Lidov–Kozai oscillations with various short-range forces, while simultaneously accounting for the radius inflation and tidal disruption of the planet. We find that a high-eccentricity migration scenario can successfully explain nearly all observed system properties. Our simulations further suggest that the initial location of WASP-107 b at the onset of migration is likely within the snowline (<0.5 au). More distant initial orbits usually lead to tidal disruption or orbit crossing. WASP-107 b most likely lost no more than 20% of its mass during the high-eccentricity migration, i.e., it did not form as a Jupiter-mass object. More vigorous tidally induced mass loss leads to disruption of the planet during migration. We predict that the current-day mutual inclination between the planets b and c is substantial: at least 25°–55°, which may be tested with future Gaia astrometric observations. Knowing the current-day mutual inclination may further constrain the initial orbit of planet b. We suggest that the proposed high-eccentricity migration scenario of WASP-107 may be applicable to HAT-P-11, GJ-3470, HAT-P-18, and GJ-436, which have similar orbital architectures.

Unified Astronomy Thesaurus concepts: Exoplanet astronomy (486); Hot Jupiters (753); Exoplanet formation (492); Exoplanet migration (2205); Exoplanet tides (497)

1. Introduction

Thanks to its large-scale height and relatively bright host star ($V = 11.5$, $J = 9.4$), WASP-107 b is arguably one of the best-characterized exoplanets to date. The host star is a K6 dwarf ($T_{\rm eff} = 4300$ K, Anderson et al. 2017) with a rotation period of 17 days. Coupled with a high chromospheric S-index of 0.90 (Baliunas et al. 1995), the star could be as young as 600 Myr old (see also Piaulet et al. 2021, who suggested a more mature age if magnetic spindown is stalled). See also Bouma et al. (2023). Planet b has a Jupiter-like radius of $0.948 \pm 0.03 R_j$ (Dai & Winn 2017) and a Neptune-like mass of $30.5 \pm 1.7 M_\oplus$ (Piaulet et al. 2021), hence an exceptionally low density of $\sim$0.1 g cm^{-3}. The planet is on a 5.7 day orbit with a nonzero eccentricity of 0.06±0.04 (Piaulet et al. 2021). There is also a distant companion on a roughly 1100 day orbit with a projected mass $M_c \sin i = 0.36 M_j$. WASP-107 b was found to be on a polar, slightly retrograde orbit with a sky-projected stellar obliquity $I_{iS} = 118^{+38}_{-19}$° (Dai & Winn 2017; Rubenzahl et al. 2021). WASP-107 b is also vigorously losing its atmosphere as revealed by metastable Helium observations (Spake et al. 2018; Allart et al. 2019; Kirk et al. 2020). The mass-loss rate is estimated to be about $1 M_\oplus$ Gyr^{-1} (Wang & Dai 2021), and a stronger-than-solar stellar wind collimates the outflow into a comet-like tail (Spake et al. 2021). More recently, Dyrek et al. (2024) reported transmission spectroscopic observations of WASP-107 b using the Mid-Infrared Instrument (MIRI) of the James Webb Space Telescope (JWST; Gardner et al. 2006). They reported clear evidence of photochemistry driven by high-energy irradiation from the host star that produced SO_2 (see also Tsai et al. 2023). There are also hints of a high-altitude (10^{-5} bar) silicate cloud that demands vigorous vertical mixing. Welbanks et al. (2024) performed a panoramic analysis of all available transmission spectroscopy of WASP-107 b from Hubble (Kreidberg et al. 2018), MIRI (Dyrek et al. 2024), and JWST/NIRCam. Welbanks et al. (2024) suggest that WASP-107 b must be internally heated with an intrinsic temperature $T_{\rm int} > 345$ K. They also found a strong vertical mixing rate $\log[K_{zz}/({\rm cm^2\ s^{-1}})] = 8.4-9$ on WASP-107 b. Welbanks et al. (2024) further reported an atmospheric metallicity that is 10–18 × solar metallicity, and a carbon-to-oxygen ratio of C/O $= 0.33^{+0.06}_{-0.05}$. Sing et al. (2024) found similar conclusions using JWST/NIRSpec data. They reported even higher planetary atmospheric metallicity of 43 ± 8 times solar, higher $T_{\rm int} = 460 \pm 40$ K, and stronger vertical mixing $\log[K_{zz}/({\rm cm^2\ s^{-1}})] = 11.6 \pm 0.1$. Compared with the host star, Hejazi et al. (2023) reported stellar abundance [Fe/H] $= -0.071 \pm 0.014$ and stellar C/O $= 0.50 \pm 0.10$.

We propose in this paper that a high-eccentricity migration (high-e migration) scenario (e.g., Fabrycky & Tremaine 2007; Dawson & Johnson 2018) can thread many observations of the WASP-107 system into a coherent story. WASP-107 b likely initially formed further out in the disk where conditions are more conducive for the accretion of a thick envelope (Lee & Chiang 2015). Secular evolution, particularly LK oscillation (Naoz 2016), induced by planet c launched planet b into an eccentric, mutually inclined, high-stellar-obliquity ($I_{iS} = 118^{+38}_{-19}$°; Rubenzahl et al. 2021) orbit around the host star. Eccentricity tidal interaction with the host star dissipates energy from the planet's orbit, causing it to slowly circularize

while the semimajor axis decreases. Today, the planet has not fully circularized yet ($e = 0.06 \pm 0.04$; Piaulet et al. 2021). Orbital energy is still being dissipated within the planet and leads to significant internal heating ($T_{\rm int} > 345$ K, Welbanks et al. 2024; $T_{\rm int} = 460 \pm 40$ K, Sing et al. 2024). The internally heated planet coupled with high-energy irradiation from a young host star drives vigorous atmospheric erosion on the planet (Spake et al. 2021; Wang & Dai 2021, $1 M_\oplus\,{\rm Gyr}^{-1}$). This hydrodynamic outflow naturally provides the necessary vertical mixing to elevate silicate clouds (10^{-5} bar; Dyrek et al. 2024) to high altitudes (see also Wang & Dai 2019).

WASP-107 is not alone, such a high-e migration scenario may be widely applicable to several hot Neptune planets with similar orbital architectures, e.g., HAT-P-11 (Bakos et al. 2010; Sanchis-Ojeda & Winn 2011; Allart et al. 2018; Xuan & Wyatt 2020), GJ-3470 (Bonfils et al. 2012; Lampón et al. 2021; Stefânsson et al. 2022), GJ-436 (Butler et al. 2004; Ehrenreich et al. 2015; Bourrier et al. 2018), HAT-P-18 (Hartman et al. 2011; Esposito et al. 2014; Paragas et al. 2021), and Kepler-1656 (Angelo et al. 2022). These planets have polar orbits around their host star; have residual orbital eccentricities; possess low-density atmospheres that may be eroding; and have more distant stellar or planetary companions (if enough long-term radial velocity monitoring is available).

In this work, we simulate directly the suspected high-e formation pathway for WASP-107 b with the aim of answering the following questions:

1. Can the observed planet c induce a high-e migration of planet b? What must be the initial mutual inclination between the two planets? How about the current mutual inclination which may be constrained with astrometric measurements (Gaia Collaboration et al. 2016)?
2. Can a high-e migration successfully reproduce the current-day polar orbit of WASP-107 b around the host star?
3. With a 5.7 day orbit around the host star, is WASP-107 b expected to be fully circularized or still experiencing eccentricity tides?
4. Did WASP-107 b start out beyond the snowline of the disk before the migration? Or was the progenitor closer in?
5. Was WASP-107 b born with a low mass ($\sim 0.1 M_J$), or could it have lost a significant portion of its mass during high-e migration?
6. When was the radius WASP-107 b inflated? Could it survive tidal disruption with an inflated radius during the migration?

The paper is structured as follows. In Section 2, we lay out the numerical setup of our simulations. We present a few case studies where high-e migration successfully produced analogs of the WASP-107 system in Section 3. We show our population synthesis results in Section 4. Finally, we conclude the findings of this paper in Section 5.

2. Simulation Setup

Our simulation leverages the well-characterized orbital architecture and planetary properties of the WASP-107 system. We stick to the observed properties of the system as much as we can, which fixes the mass and radius of the host star, the semimajor axis of the outer orbit. The key parameters we will explore are listed in Table 1. M_*, M_p, and M_c, respectively, represent the masses of the host star, the inner planet (WASP-107 b), and the outer planet (WASP-107 c). The Keplerian orbital elements of the inner planet b are without a subscript (e.g., a and e) and those for the outer planet c have a subscript "o." We also use subscripts "init" and "fin" to indicate parameters at the beginning and the end of our simulations.

Table 1
Parameters We Sample for the Population Synthesis Study

Parameter	Meaning	Range
$M_{p,\rm init}/M_j$	Initial inner planet mass	(0.1, 0.5)
$R_{p,\rm init}/R_j$	Initial planet radius	(0.6, 1.5)
$a_{\rm init}$/au	Initial inner semimajor axis	(0.15, 0.5)
M_c/M_j	Outer planet mass	(0.36, 1.5)
$\cos I_{io,\rm init}$	Initial i-o inclination	(−0.9, 0.75)
$e_{o,\rm init}$	Initial outer eccentricity	(0.2, 0.45)[a]
$\phi_{o,\rm init}$	Outer argument of periastron	(0, 2π)
lg$A$	Tidal mass-loss rate; see Equation (14)	(2.8, 5)
lg$\tau_{\rm inf}$	Inflation timescale in Myr (Equation (24))	(0, 2.5)

Notes. All of them are sampled uniformly within the specified range.
[a] We sample e_{o0} only when the octupole LK is used. For quadrupole LK, we fix $e_o = 0.28$.

2.1. Lidov–Kozai Oscillation Including Octupole Terms

We evolve numerically the M_*-M_p-M_c triple system under the LK oscillation (also known as the von Zeipel–Lidov–Kozai; von Zeipel 1910; Kozai 1962; Lidov 1962). We also include short-range forces due to GR, tides, and rotation-induced quadrupole of the star and the planet. Our numerical setup closely follows the pioneering work of Anderson et al. (2016; see also Vick et al. 2019). A notable improvement is that we incorporated the backreaction on the outer orbit at the octupole order based on Liu et al. (2015). We will compare and contrast the simulations with and without including the octupole LK terms (Naoz et al. 2011, 2012, 2013; Albrecht et al. 2012; Li et al. 2014a, 2014b; Antognini 2015; Liu et al. 2015; Petrovich 2015; Anderson et al. 2016; Naoz 2016; Petrovich & Tremaine 2016; Stephan et al. 2016, 2017, 2018; Storch et al. 2017; Liu & Lai 2018; Vick et al. 2019). Simulations evolved with the octupole terms are dubbed "octLK," and those including only quadrupole terms are "quaLK." In both cases, we average over both the inner and outer orbits. Also incorporated in our simulation are the mass loss from the planet and radius inflation; see, respectively, Sections 2.2 and 2.3.

Before proceeding, we briefly review the properties of the LK dynamics, which can be largely derived analytically when restricted to the quadrupole order. Conservation of the total angular momentum and total energy (to the quadrupole order) leads to the relation (Liu et al. 2015; Anderson et al. 2016; Liu & Lai 2018)

$$\frac{3}{8}\frac{e_{\rm max}^2}{j_{\rm min}^2}\left[5\left(c_{io}+\frac{\eta}{2}\right)^2-\left(3+4\eta c_{io}+\frac{9}{4}\eta^2\right)j_{\rm min}^2+\eta^2 j_{\rm min}^4\right]+\epsilon_{\rm GR}\left(\frac{1}{j_{\rm min}}-1\right)+\frac{\epsilon_{\rm ST}}{15}\left(\frac{1+3e_{\rm max}^2+\frac{3}{8}e_{\rm max}^4}{j_{\rm max}^9}-1\right)=0, \quad (1)$$

where $c_{io} = \cos I_{io,\rm init}$ is the cosine of the initial inclination between the inner and outer orbit and $e_{\rm max} = \sqrt{1-j_{\rm min}^2}$. The

smallest pericenter separation can be calculated from $e_{\max}$ as $r_{p,\min} = a(1-e_{\max})$. Following Liu & Lai (2018), we have introduced

$$\eta = \left(\frac{L}{L_o}\right)_{e=0} = \frac{\mu}{\mu_o}\left[\frac{(M_*+M_p)a}{(M_*+M_p+M_c)a_o(1-e_o^2)}\right]^{1/2}, = 0.052\left(\frac{\mu}{0.12\,M_\odot}\right)\left(\frac{\mu_o}{0.8\,M_\odot}\right)^{-1} \times \left(\frac{M_*+M_p}{M_*+M_p+M_c}\right)^{1/2} \times \left(\frac{a}{0.2\text{ au}}\right)^{1/2}\left(\frac{a_o(1-e_o^2)}{1.7\text{ au}}\right)^{1/2}, \quad (2)$$

to characterize the strength of the backreaction of the inner orbit on the outer one, with $\mu = M_pM_*/(M_*+M_p)$ and $\mu_o = M_c(M_*+M_p)/(M_*+M_p+M_c)$. Also introduced are

$$\epsilon_{\rm GR} = \frac{3G(M_*+M_p)^2a_{\rm o,eff}^3}{c^2M_ca^4}, = 6.4\times10^{-2}\left(\frac{M_*+M_p}{0.69\,M_\odot}\right)^2\left(\frac{M_c}{0.8\,M_j}\right)^{-1} \times \left(\frac{a_{\rm o,eff}}{1.77\text{ au}}\right)^3\left(\frac{a}{0.2\text{ au}}\right)^{-4}, \quad (3)$$

$$\epsilon_{\rm ST} = \frac{15k_{2p}M_*(M_*+M_p)a_{\rm o,\,eff}^3R_p^5}{M_pM_ca^8}, = 1.2\times10^{-3}\left(\frac{k_{2p}}{0.37}\right)\left(\frac{M_p}{0.12\,M_j}\right)^{-1}\left(\frac{R_p}{0.94\,R_j}\right)^5 \times \left(\frac{M_*}{0.69\,M_\odot}\right)\left(\frac{M_*+M_p}{0.69\,M_\odot}\right)\left(\frac{M_c}{0.8\,M_j}\right)^{-1} \times \left(\frac{a}{0.2\text{ au}}\right)^{-8}\left(\frac{a_{\rm o,eff}}{1.77\text{ au}}\right)^3, \quad (4)$$

to characterize the strength of short-range forces due to general relativity (GR) and static tide (ST). In the equations above, $a_{\rm o,\,eff} = a_o\sqrt{1-e_o^2}$, and a is evaluated at its initial value $a_{\rm init}$ (as we ignore tidal dissipation for now and assume energy is conserved). Numerical values are provided for typical parameters that describe the WASP-107 system. In the limit where $\eta = \epsilon_{\rm GR} = \epsilon_{\rm ST} = 0$, Equation (1) reduces to the well-known condition $e_{\max} = \sqrt{1-(5/3)c_{io}^2}$.

It is also instructive to consider the limiting eccentricity (or $j_{\rm lim}^2 = 1-e_{\rm lim}^2$) reached when only one of ($\epsilon_{\rm GR}$, $\epsilon_{\rm ST}$) is nonzero and the backreaction η is ignored. Approximately, we can set $e_{\max}\simeq 1$ and $c_{io}\simeq 0$, leading to a simple relation (Anderson et al. 2016)

$$\frac{\epsilon_{\rm GR}}{j_{\rm lim}} + \frac{7\epsilon_{\rm ST}}{24j_{\rm lim}^9} \simeq \frac{9}{8}. \quad (5)$$

When GR dominates, we have

$$j_{\rm lim}^2|_{\rm GR} \simeq \frac{64}{81}\epsilon_{\rm GR}^2 \simeq 3.2\times10^{-3}\left(\frac{a}{0.2\text{ au}}\right)^{-8}, \quad (6)$$

while the ST-dominated case leads to

$$j_{\rm lim}^2|_{\rm ST} \simeq \left(\frac{7}{27}\epsilon_{\rm ST}\right)^{2/9} \simeq 0.17\left(\frac{a}{0.2\text{ au}}\right)^{-16/9}. \quad (7)$$

The same numerical values used in Equations (3) and (4) are adopted to arrive at the numerical estimations of $j_{\rm lim}$, and we have only kept the scaling with respect to a explicitly as it represents one of the largest uncertainties in the system and we will aim to constrain it in Section 4.3. As the greater of Equations (6) and (7) determines $j_{\rm lim}$, it is typically ST that limits the maximum eccentricity excitation for WASP-107-like systems to around $e_{\max}\simeq 0.91$. When the backreaction cannot be ignored, the maximum eccentricity is not achieved at $c_{\rm io} = 0$ ($I_{io,\rm init} = 90°$) but instead at (noting that Equation (1) describes a quadratic function with respect to c_{io})

$$c_{io,\rm lim} = \frac{\eta}{2}\left(\frac{4}{5}j_{\rm lim}^2 - 1\right) \simeq -\frac{\eta}{2} \simeq -0.026\left(\frac{a}{0.2\text{ au}}\right)^{1/2}. \quad (8)$$

In other words, the limiting eccentricity is achieved when the initial inclination between the inner and outer orbits is $I_{io,\rm init}\simeq 91.^\circ5$. Consequently, an initially retrograde orbit in general experiences a stronger LK excitation than a prograde one does.

Our prescription for tidal dissipation follows the ST model introduced by Hut (1981). The dissipation is parameterized through a constant time lag $t_{\rm lag}$ that is inversely proportional to the tidal quality factor Q. The characteristic decay timescale is (Vick et al. 2019)

$$t_t^{-1} = \left(\left|\frac{\dot a}{a}\right|\sqrt{1-e^2}\right)_{e_{\max}} = 6k_{2p}t_{\rm lag}\frac{M_*}{M_p}\left(\frac{R_p}{a}\right)^5\frac{n^2}{(1-e^2)^7}\left[f_1(e) - \frac{f_2^2(e)}{f_5(e)}\right], \quad (9)$$

where k_{2p} is the planetary Love number and $n = 2\pi/P$ is the mean motion; $f_{1,2,5}(e)$ are functions of eccentricity defined in Hut (1981). An additional factor of $\sqrt{1-e_{\max}^2}$ is included in the timescale estimation because the time the planet spends at $e\simeq e_{\max}$ is only a fraction of $\sqrt{1-e_{\max}^2}$ of the LK oscillation period. We consider here only the planetary dissipation; the stellar dissipation is smaller by a factor of $(M_*/M_p)^2(R_p/R_*)^5\sim 3\times10^3$ the values for k_2 and $t_{\rm lag}$ are similar. We assume $t_{\rm lag} = 10$ s as the default value in our simulations. Such a choice is motivated by the quality factor of our ice giants $Q\simeq 10^4$ (see recent results on Uranus, Gomes & Correia 2024), while Jupiter-mass planets have $Q = 10^5$–10^6 (Wu 2005; Millholland 2019 and references therein). To produce the vigorous internal heating of WASP-107 b with an internal temperature of 345 K (Welbanks et al. 2024), or equivalently a tidal heating rate of $L_t\simeq 10^{-7}L_\odot$, $t_{\rm lag}\simeq 10$ s also required (see

later in Equation (22)).[3] Correspondingly, the time lag for Jupiter is $t_{\rm lag} \simeq 0.1$ s, and Anderson et al. (2016) adopted $t_{\rm lag} = 1$ s during their high-e migration simulations. For completeness, we will also consider the case where $t_{\rm lag} = 1$ s in Section 4.6.

A window for successful migration within a given time can be defined once the tidal lag time $t_{\rm lag}$ is specified. One can equate the migration timescale and the age of the system (which we assume to be 600 Myr for WASP-107 b–like systems). This leads to a requirement on the pericenter separation (Vick et al. 2019)

$$r_p \lesssim r_{p,\rm mig} = 0.040\ {\rm au}\left(\frac{M_*}{0.69\,M_\odot}\right)^{2/7}\left(\frac{a_{\rm init}}{0.2\ {\rm au}}\right)^{-1/7} \times\left(\frac{M_p}{0.12\,M_j}\right)^{-1/7}\left(\frac{R_p}{0.94\,R_j}\right)^{5/7}\left(\frac{k_{2p}}{0.37}\right)^{1/7} \times\left(\frac{t_t}{600\ {\rm Myr}}\right)^{1/7}\left(\frac{t_{\rm lag}}{10\ {\rm s}}\right)^{1/7}, \quad (10)$$

for the planet to be able to migrate within its age, where $r_{p,\rm mig}$ denotes the critical value of r_p for the planet to migrate. Under quaLK, the pericenter separation further translates to a window on the required initial inclination between the inner and outer orbit, $I_{io,\rm init}$. As Equation (1) is quadratic in c_{io}, its roots can be easily computed from

$$c_{io,\rm mig} = \frac{-\mathcal{B} \pm \sqrt{\mathcal{B}^2 - 4\mathcal{A}\mathcal{C}}}{2\mathcal{A}}, \quad (11)$$

where

$$\mathcal{A} = \frac{15}{8}\frac{e_{\rm max}^2}{j_{\rm min}^2}, \quad \mathcal{B} = \frac{3}{8}\frac{e_{\rm max}^2}{j_{\rm min}^2}\eta(5 - 4j_{\rm min}^2),$$
$$\mathcal{C} = \frac{3}{8}\frac{e_{\rm max}^2}{j_{\rm min}^2}\left[\frac{5}{4}\eta^2 - (3 + \frac{9}{4}\eta^2)j_{\rm min}^2 + \eta^2 j_{\rm min}^4\right] + \epsilon_{\rm GR}\left(\frac{1}{j_{\rm min}} - 1\right) + \frac{\epsilon_{\rm ST}}{15}\left(\frac{1 + 3e_{\rm max}^2 + \frac{3}{8}e_{\rm max}^4}{j_{\rm max}^9} - 1\right),$$

with

$$e_{\rm max}^2 = 1 - j_{\rm min}^2 \equiv \left(1 - \frac{r_{p,\rm mig}}{a_{\rm init}}\right)^2.$$

We emphasize that the estimation above applies only to the quaLK systems. The relative importance of the octupole term can be quantified by the parameter (Liu et al. 2015)

$$\epsilon_{\rm oct} = \frac{M_* - M_p}{M_* + M_p}\frac{a}{a_o(1 - e_o^2)}e_o = 0.033\left(\frac{M_* - M_p}{M_* + M_p}\right)\left(\frac{a}{0.2\ {\rm au}}\right)\left(\frac{a_o(1 - e_o^2)}{1.7\ {\rm au}}\right)^{-1} \times\left(\frac{e_o}{0.28}\right), \quad (12)$$

which can be significant for the WASP-107 system. As we will see later in Section 4.2 (and consistent with previous analyses; e.g., Liu et al. 2015; Petrovich 2015; Naoz 2016), octLK enables a much wider merger window in general with the addition of the octupole potential.

Throughout our simulations, we make a few simplifying assumptions: the inner planet's spin is instantaneously pseudosynchronized (Hut 1981) and aligned with the inner orbit. We fixed the stellar rotation period at the currently measured $P_* = 17.2$ days (Dai & Winn 2017). This relatively long period suggests that the precession rate induced by stellar rotation is typically 20 times smaller than that due to GR (see, e.g., Equations (A8) and (A10) of Anderson et al. 2016). Moreover, the characteristic spindown timescale (denoted with a subscript "sd") for the host star due to magnetic breaking is (Barker & Ogilvie 2009; Anderson et al. 2016)

$$\tau_{\rm sd} = \frac{1}{\alpha\Omega_*^2} \simeq 3.7\ {\rm Gyr}\left(\frac{\alpha}{1.5\times10^{-14}\ {\rm yr}}\right)^{-1}\left(\frac{P_*}{17.2\ {\rm days}}\right)^2. \quad (13)$$

The fiducial value of α is taken from Barker & Ogilvie (2009) for K stars (see also Curtis et al. 2019). This is much greater than the migration timescale, and hence the stellar spindown is insignificant. We separately verified this through a set of numerical simulations including the spindown which shows little difference from the main results we present. The direction of the stellar spin vector $\boldsymbol{S}_*$, however, precesses due to its interaction with the orbital angular momentum (see Appendix A2 of Anderson et al. 2016). Following the precession of the stellar rotation is important for calculating the stellar obliquity, which is an observed quantity for WASP-107 b (Rubenzahl et al. 2021).

2.2. Tidally Driven Mass Loss and Disruption

During a high-e migration, the close pericenter passage of the planet makes it venture to tidal disruption by the host star. Motivated by numerical simulations performed by Guillochon et al. (2011), Anderson et al. (2016) used a hard boundary to capture the disruption. Whenever the pericenter separation r_p is less than $2.7r_t$ ($r_t \equiv R_p(M_*/M_p)^{1/3}$ is the tidal radius), the migrating planet is considered to be instantaneously and fully disrupted. We include a more flexible tidally driven mass-loss prescription than that adopted by Anderson et al. (2016). A key question we would like to address is whether WASP-107 b could have started as a much more massive planet (say Jupiter-mass), and was subsequently reduced to its observed Neptune-like mass during the postulated high-e migration by *partial* disruption. Guillochon et al. (2011) have performed extensive 3D hydrodynamical simulations of multiorbit encounters of a migrating hot Jupiter with the host star with a pericenter close to a few times the tidal radius. Guillochon et al. (2011) found that the mass loss in each close encounter is roughly exponentially related to the pericenter distance normalized by the tidal radius:

$$\Delta M_p^{(1\ {\rm pass})}/M_p = -A\,{\rm Exp}[-B(r_p/r_t)] < 0, \quad (14)$$

where A and B are coefficients of a phenomenological fit to their hydrodynamic simulations of mass loss (see their Figure 10). We stress that this mode of mass loss is primarily due to

[3] As a caveat, this estimation assumes that all the internal heating is caused by instantaneous tidal heating. The mean tidal heat rate averaged over the migration can be estimated by dividing the current orbital binding energy by the age of the system, leading to $\langle L_t\rangle \simeq 2\times10^{-7}L_\odot$. If the migration time is shorter, the mean heating rate can be even higher. The residual of this may also contribute to the observed heating, and we leave this possibility to future investigations.

the quick growth and breakup of the dynamical tides on the planet at $r_p > 2r_t$ (Mardling 1995; Ivanov & Papaloizou 2004, 2007; Vick & Lai 2018; Wu 2018; Yu et al. 2021, 2022) rather than direct Roche lobe overflow (which happens at $r_p \approx 2r_t$ when $M_p \ll M_*$; Eggleton 1983). While the mass loss at each close encounter can be highly stochastic, we use Equation (14) to approximate the averaged effect. The value of B is set to $B = 9.25$, corresponding to the sharp dependence of the dynamical tide on the pericenter distance. The slope is consistent with the solid orange line in Figure 10 of Guillochon et al. (2011). We leave parameter A as a free variable to be explored during the simulations. It is sampled log-uniformly from the range $A \sim 10^3$–10^5, corresponding to a 10^{-8}–10^{-6} fractional mass loss per pericenter passage. As we will see later, A effectively controls the boundary between disruption and survival of the migrating planet. The range we assume reproduces the survival threshold found in Guillochon et al. (2011) while allowing partial disruptions of the planet. While most of the mass loss occurs near periastron passage, we can estimate the orbital averaged rate as

$$\dot{M}_p = \frac{\Delta M_p^{(1\ \mathrm{pass})}}{P}, \tag{15}$$

where P is the orbital period. For simplicity, we fix the planetary radius when its mass changes, an assumption appropriate if the planet's equation of state can be approximated by a $p \propto \rho^2$ polytrope.

We further note that both the tidal radius r_t and the pericenter distance r_p may evolve as a result of the mass loss in the previous passage. The tidal radius r_t changes because the density of the planet adjusts after the mass loss. If the density of the planet decreases, the tidal radius r_t increases (the surface gravity of the planet is weaker and the planet is more loosely bound). The next encounter will lead to more intensive mass loss. As such, the planet may enter a runaway mass loss, i.e., disruption.

Mass loss may change the orbit of the planet as well. Here we consider two limiting cases. The first limiting case is the so-called conservative mass transfer frequently used when one object in a binary overfills its Roche lobe (Sepinsky et al. 2007). Here the host star and WASP-107 b are treated like a binary system, whose total mass and total orbital angular momentum are conserved. If so, we have (Sepinsky et al. 2007)

$$\left(\frac{\dot{a}}{a}\right)_{\mathrm{MT,con}} = 2\frac{1+e}{1-e}\left(\frac{M_p}{M_*} - 1\right)\frac{\dot{M}_p}{M_p}, \tag{16}$$

$$\dot{e}_{\mathrm{MT,con}} = (1-e)\left(\frac{\dot{a}}{a}\right)_{\mathrm{MT,\ con}}. \tag{17}$$

The equations above also assume that mass transfer happens instantaneously at the pericenter, and we ignore finite-size effects. Sepinsky et al. (2007) suggest that the mass transfer creates only a torque without a radial acceleration (see their Equations (B5), (B6), and (B16–18)). Consequently, it does not lead to pericenter precession and we have $\dot{\boldsymbol{e}}_{\mathrm{MT,\ con}} = \dot{e}_{\mathrm{MT,\ con}}\hat{\boldsymbol{e}}$. We will refer to this scenario as "conservative mass transfer" with the subscript "con."

However, Guillochon et al. (2011) suggest that the host star may accrete only a small fraction of the mass loss from the planet. Furthermore, it is unclear if the mass accreted by the host star can quickly transfer the angular momentum it carries back to the orbit of the planet. As another limiting case, we assume the orbit loses all of the angular momentum carried by the mass loss:

$$\left(\frac{j}{J}\right)_{\mathrm{MT,non-con}} = \frac{\dot{M}_p}{M_p}. \tag{18}$$

Because $M_* \gg M_p$, we simply set $\dot{a}_{\mathrm{MT,non-con}} = \dot{e}_{\mathrm{MT,non-con}} = 0$. We will refer to this prescription as "nonconservative mass loss." We note that neither prescription is perfect; the reality is most likely somewhere in between. Yet given the nature of simulations done by Guillochon et al. (2011), the nonconservative scenario may be more favored. As we will see later, the formation of a WASP-107 b–like planet also favors the nonconservative limit.

Similar to the migration window defined in Equations (10) and (11), the requirement for the planet to survive disruption also constrains the allowed range on r_p and further $I_{io,\mathrm{init}}$. As we will see later, the requirement can be written as

$$r_p \gtrsim r_{p,\mathrm{dis}} \equiv c_{\mathrm{dis}} r_t, \tag{19}$$

where c_{dis} is a numerical constant ($c_{\mathrm{dis}} \simeq 2.7$ based on Guillochon et al. 2011 and our choice of A in Equation (14) explores the range $c_{\mathrm{dis}} \in [2, 3]$). In terms of $I_{io,\mathrm{init}}$, the window can be obtained using again the quadratic formula in Equation (11) but this time with $e_{\max} = 1 - r_{p,\mathrm{dis}}/a_{\mathrm{init}}$. Therefore, a successful migration requires the pericenter separation to satisfy $r_{p,\mathrm{dis}} \lesssim r_p \lesssim r_{p,\mathrm{mig}}$.

2.3. Radius Inflation

The radius of WASP-107 b is inflated. The planet has a Jupiter-like radius of $0.948 \pm 0.03\ R_j$ (Dai & Winn 2017) while its mass is only 10% of that of Jupiter: $30.5 \pm 1.7 M_\oplus$ (Piaulet et al. 2021). The mean density of $\sim 0.1\ \mathrm{g\ cm^{-3}}$ is a whole order of magnitude lower than Jupiter's. To address the possibility of radius inflation, we incorporate a prescription following Thorngren et al. (2021) for a subset of our simulations. The equilibrium radius of the planet is given by:

$$R_{\mathrm{eq}} = 1.21 R_j \left(\frac{M_p}{M_j}\right)^{-0.045} \times \left(\frac{F}{10^9 \mathrm{erg\ s^{-1}\ cm^{-2}}}\right)^{0.149 - 0.072 \lg(M_p/M_j)}, \tag{20}$$

with the effective flux F given by

$$F = F_{\mathrm{irr}} + F_t = \frac{L_*}{4\pi r_{\mathrm{eff}}^2} + \frac{L_t}{4\pi R_p^2}. \tag{21}$$

We have $1/r_{\mathrm{eff}}^2 = 1/(a^2\sqrt{1-e^2})$, which preserves the insolation averaged over each orbit. We have also added the tidal heating,

$$L_t = 3 k_{2p} t_{\mathrm{lag}} n^2 \left(\frac{GM_*^2}{R_p}\right)\left(\frac{R_p}{a}\right)^6 \frac{\left[f_1(e) - \frac{f_2^2(e)}{f_5(e)}\right]}{(1-e^2)^{15/2}}, \tag{22}$$

assuming that it is evenly distributed throughout the planet. We note that $R_{\mathrm{eq}} = 0$ when $F = 0$ in this simple prescription.

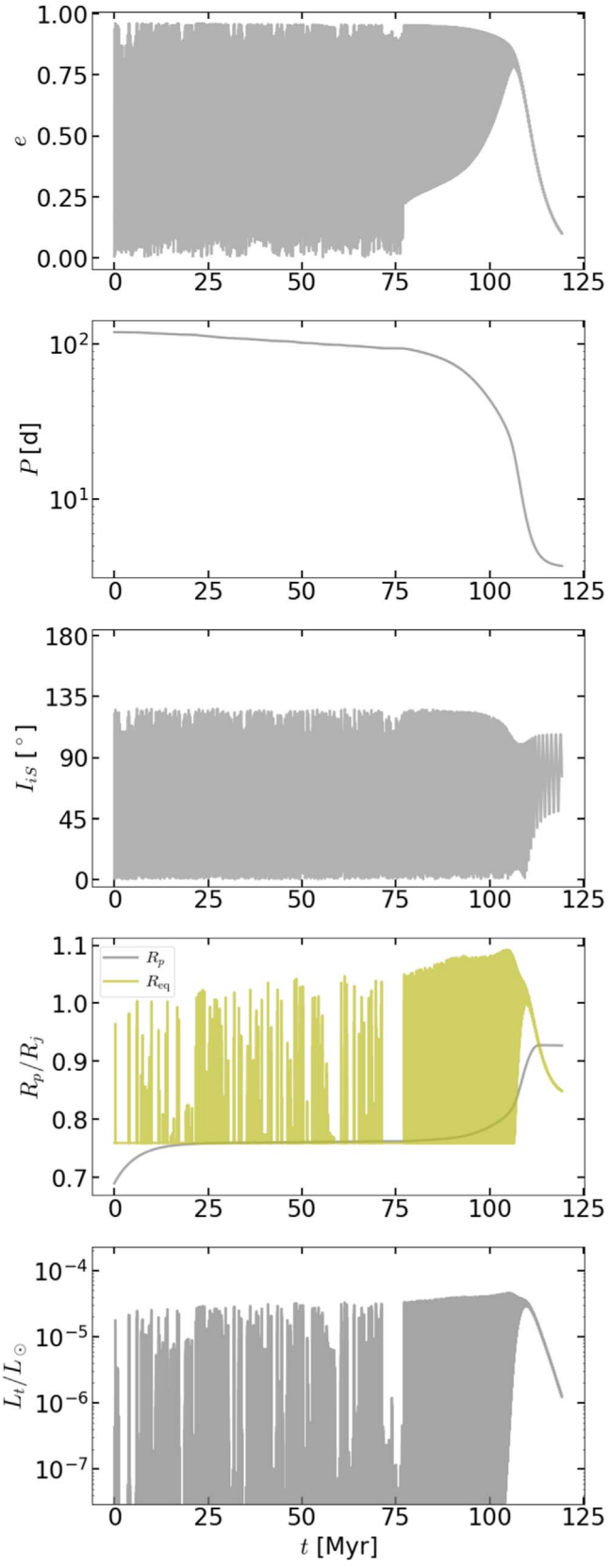

Figure 1. Evolution trajectory of a potential WASP-107 b progenitor. From top to bottom, we show the orbital eccentricity, orbital period, stellar obliquity, planetary radius, and tidal heating luminosity. This high-e migration reproduces multiple observable features of WASP-107 b: it successfully migrated from an initial orbital period >100 days to an orbital period <5 days in ∼100 Myr with an inflated radius and nearly polar obliquity. The current tidal heating can be as high as $10^{-6}L_\odot$.

Therefore, we add a lower limit on the equilibrium radius using the mass of the planet and the empirical mass–radius relationship (Chen & Kipping 2017). When the instantaneous planetary radius deviates from the equilibrium radius, it evolves over time according to

$$\frac{dR}{dt} = \frac{R_{\rm eq} - R}{\tau}, \tag{23}$$

$$\tau = \begin{cases} \tau_{\rm def}, & R > R_{\rm eq}, \\ \tau_{\rm inf}, & R < R_{\rm eq}. \end{cases} \tag{24}$$

The timescales $\tau_{\rm def}$ and $\tau_{\rm inf}$ separately controls the deflation and inflation timescale of the planet. The deflation timescale is most likely comparable to or longer than the duration of our simulation. Thorngren et al. 2021 found evidence for delayed cooling, and they used $\tau_{\rm def} = 0.5$ Gyr. We similarly adopted $\tau_{\rm def} = 0.5$ Gyr. On the other, the inflation timescale is much more critical in our study. Thorngren et al. 2021 found evidence for rapid reinflation of hot Jupiters. We thus uniformly sampled $\lg(\tau_{\rm inf}/{\rm Myr})$ between 0 and 2.5 when the planetary radius is allowed to change. We do not consider greater values of $\tau_{\rm inf}$ as it changes the radius by little. This is equivalent to turning off radius evolution, which we do for another subset of our simulations. Furthermore, we find our radius inflation prescription affects only the final planetary radius but has weak impacts on the other properties of the system. The reason is that a significant radius inflation can happen only near the end of the migration where the inner binary and the perturbing planet have decoupled. We will discuss this in more detail in Section 3 when we examine specific examples. As a caveat, we note that the results of Thorngren et al. (2021) were calibrated only for planets with $M_p > 0.5\,M_j$. We have extrapolated their results to $M_j \in (0.1, 0.5)M_j$, which is the regime we are studying here for WASP-107 b. We have compared the results with and without radius inflation, and the qualitative conclusions of this paper remain consistent. Future work with a more elaborate radius inflation model in the $M_j \in (0.1, 0.5)M_j$ regime should help improve our results.

3. Case Study

We performed a population synthesis study to explore how different initial conditions and system parameters determine the formation of WASP-107 b–like systems. The parameters we sampled and their ranges are shown in Table 1. Before talking about the population-level outcome of our simulations, let us first examine some specific examples.

Figure 1 shows the evolution track for a particular simulation that reproduces multiple observed properties of WASP-107 b. From top to bottom, we show the evolution of the inner planet's orbital eccentricity e, orbital period P, the stellar obliquity, the planet radius R_p, and the luminosity due to eccentricity tides L_t. The system is evolved with octupole LK oscillations and nonconservative mass loss. The initial planet mass is $0.25\,M_j$ and stays nearly constant during the evolution. In other words, mass loss was minimal during the whole migration process. The inner planet has an initial orbit of $a_{\rm init} = 0.42$ au and initial $e_{\rm init} = 0.01$. The star's spin vector $\boldsymbol{S}_*$ is initially aligned with the inner orbital angular momentum

vector $\boldsymbol{J}$. The outer orbit has $M_c = 0.62\,M_j$, $e_{o,\rm init} = 0.33$, and the initial mutual inclination between planet b and c is $I_{io,\rm init} = 64°$.

The high-e migration can be broken into three stages. When $t < 75$ Myr, the inner planet experiences eccentricity excitation through the LK cycle. Because of the octupole terms, the eccentricity excitation exhibits stochasticity (Li et al. 2014a; Liu et al. 2015). The pericenter r_p occasionally reaches very close to the host star. Whenever this happens, the eccentricity tide is strongly amplified, leading to spikes in the tidal luminosity and equilibrium planet radius in the last two panels of Figure 1. However, the radius of the inner planet stays more or less constant during this stage, because the planet is still far from the host star for most of the orbit. The orbit-averaged insolation and tidal heating are not strong enough to consistently inflate the planet. We assume an inflation timescale of $\tau_{\rm inf} = 5.8$ Myr in this particular simulation.

The second stage of the high-e migration is roughly between 75 Myr $< t <$ 110 Myr. Here, the semimajor axis of the planet has decayed so much that short-range forces (including relativity, the conservative planetary tide, and rotation-induced quadrupoles in both the star and the planet) become more significant and quenched the octupole LK effects (see Section 3.1 in Anderson et al. 2016 for more detailed discussions; also Fabrycky & Tremaine 2007; Liu et al. 2015). However, quadrupole LK effects remain important, and the eccentricity oscillation becomes regular with a gradually shrinking range. The pericenter distance of the planet follows a well-defined envelope, which is reflected in the envelope of the tidal heating rate. The orbital period of the planet declines steadily as shown in the second panel.

Finally, at around $t \simeq 110$ Myr, the orbital decay timescale becomes shorter than the LK oscillation timescale, and the inner planet decouples from the secular influence of the outer planet. The inner orbit evolves under the influence of eccentricity tides. The inner planet circularizes along a trajectory with nearly constant orbital angular momentum, so P and e decrease while the pericenter separation r_p gradually increases.

The peak of tidal heating and radius inflation happened between 100 Myr $< t <$ 110 Myr when the orbital semimajor axis had decayed significantly, amplifying the insolation from the host star. Meanwhile, the orbit stays eccentric enough that the pericenter separation r_p stays near its minimum, thereby boosting the tidal heating rate. It is the combination of intense irradiation and tidal heating that inflated the planet by about 20% during this time from $0.76R_{\rm j}$ to $0.93\ R_{\rm j}$ similar to the observed value. Inflation at this late stage is also crucial for the planet to survive the migration early on. The long deflation timescale $\tau_{\rm def} = 500$ Myr allows the planet to stay inflated even though tidal heating is lower at the very end of the simulation than during the peak of tidal heating between 100 Myr $< t <$ 110 Myr.

Meanwhile, the obliquity is attracted to around 90° after decoupling from the perturber (third panel). This is due to the dynamical attractor discussed in Liu & Lai (2018) and Yu et al. (2020). The effective axis around which the stellar spin precesses changes from the outer orbital angular momentum during the LK cycle to the inner orbital angular momentum when the inner orbit decouples from the perturber, with the opening angle being nearly constant during the transition. This produces a final obliquity consistent with observations (Dai & Winn 2017; Rubenzahl et al. 2021).

We terminate the simulation when the inner eccentricity reaches 0.1. The inner orbital period decays to 3.7 days. The tidal heating rate is smaller than its peak value by nearly two orders of magnitude yet can still be significant at a level of $10^{-6}\,L_\odot$.

A keen reader may ask, what if the inner planet ventures closer to the host star during that initial stage of migration where octupole LK oscillation stochastically excites the orbital eccentricity? Could WASP-107 b lose significant mass at this stage? Yes, and we now present a case where WASP-107 b might lose substantial mass during its high-e migration in Figure 2. The initial conditions for this system are $(M_p, R_p, a, M_c, e_o, I_{io})_{\rm init} = (0.20M_j,\ 0.78R_j,\ 0.46\,{\rm au},\ 1.1\,M_j, 0.20,\ 70°)$. A new panel showing the evolution of planetary mass M_p is added to the figure. We also show the pericenter separation normalized by the tidal radius. Notice that the whole high-e migration happens on a much faster timescale here ~10 Myr rather than the ~100 Myr in the previous example. This is because as the pericenter distance of planet b comes closer to the host star, the strong tides speed up the inward migration. Also, the strong tides unbind a fraction of the planet episodically whenever r_p/r_t is small. The orbit stays at such a small r_p only momentarily due to the stochastic nature of the octupole LK oscillation. The planet thus could avoid a runaway disruption (see first four panels of Figure 2). Besides the initial LK cycles, mass loss can also happen in another epoch near the end of the migration (around $t = 12$ Myr in the example shown). The pericenter separation stays small while the orbital period decreases rapidly, which enhances the mass-loss rate according to Equation (15). Radius inflation may also happen at the same time, keeping r_p/r_t small even if the physical r_p increases as the binary circularizes. The integrated mass loss over the entire high-e migration is about 20% of the initial mass. We will show with population synthesis in the next section that >20% mass loss usually results in a runaway disruption of the planet. The short ~10 Myr requires that the high-e migration was only recently initiated on WASP-107 b. Such a delayed migration may happen if planets b and c were only recently scattered into sufficiently inclined orbits; see, e.g., Lu et al. (2024).

4. Population Study

We run about 2×10^5 simulations to understand the probability of the high-e migration scenarios for the WASP-107 system, and how the initial system parameters translate to the testable observables at the end of the simulation. Table 1 summarizes the relevant initial parameters and their prior region. Including radius inflation or not does not impact significantly the formation rate and other population properties, because inflation happens only after the inner binary decouples from the outer planet. Therefore, in the results below we focus on the case where R_p is kept constant throughout the evolution. We note that within quaLK, one can show that

$$\boldsymbol{e}_o \cdot \left(\frac{d\boldsymbol{e}_o}{dt}\right)_{\rm quaLK} = 0. \tag{25}$$

Therefore, for quaLK runs, one can fix the eccentricity of the outer planet at its currently observed value $e_o = 0.28$ (Piaulet et al. 2021). After including octupole LK terms, however, e_o is

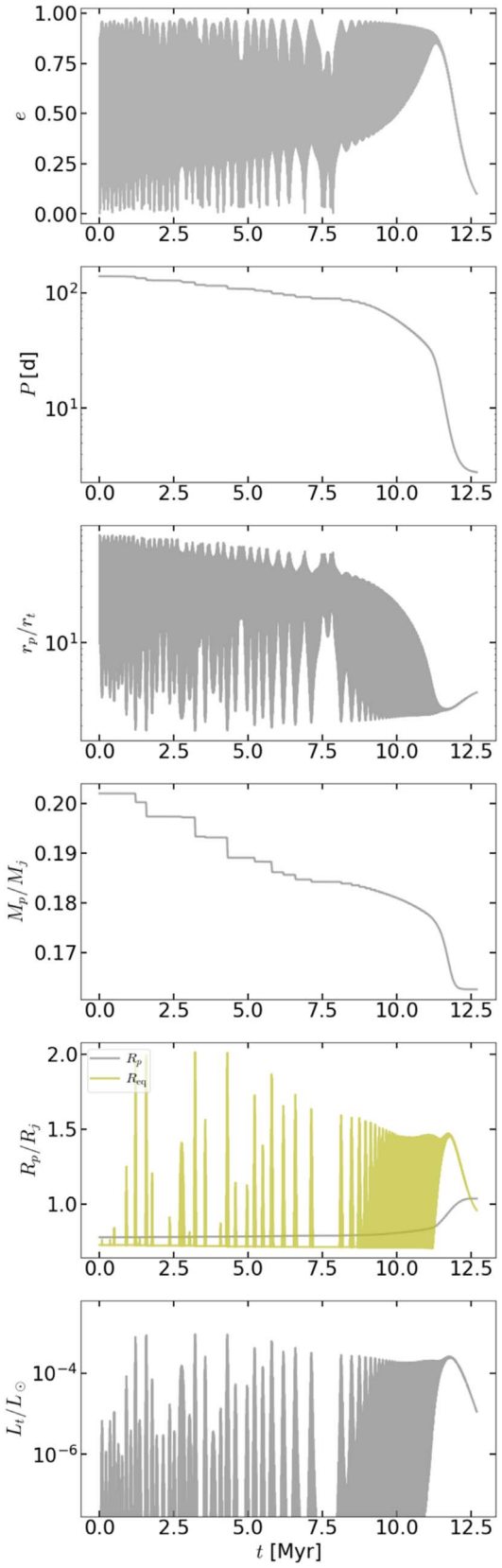

Figure 2. Similar to Figure 1 but for a system that experiences substantial mass loss (fourth panel). The planet has $M_{p0} = 0.20\,M_j$ initially and loses $0.04\,M_j$ of its mass during the migration. This is one of the cases where WASP-107 b might lose significant mass. A stronger mass loss likely leads to disruption of the planet.

no longer a constant and we sample its initial value uniformly between 0.2 and 0.45 near the measured value of 0.28 ± 0.07 (Piaulet et al. 2021). The outer eccentricity typically decreases during migration as the LK oscillation transfers angular momentum from the inner orbit to the outer one. Therefore, we do not consider cases where $e_{o,\rm init} < 0.2$.

We set the coordinates such that the initial angular momentum vector of the outer planet $\hat{\boldsymbol{J}}_{o,\rm init}$ is along the $\hat{z}$-axis, and the Cartesian components of the inner angular momentum are $\hat{\boldsymbol{J}}_{\rm init} = (\sin \iota_{io,\rm init}, 0, \cos \iota_{io,\rm init})$, where $\iota_{io,\rm init}$ is the initial mutual inclination between the inner and outer orbits. The spin vector of the host star is assumed to be aligned with the inner planet's orbital axis, $\hat{\boldsymbol{S}}_{*,\rm init} = \hat{\boldsymbol{J}}_{\rm init}$. We will denote the obliquity as I_{iS} with $\cos I_{iS} = \hat{\boldsymbol{J}} \cdot \hat{\boldsymbol{S}}_*$. Vick et al. (2023) suggest that the stellar obliquity can be excited by the protoplanetary disk before the onset of the LK oscillation. We defer investigations of this possibility to future studies. We initialize the outer eccentricity as $\boldsymbol{e}_{o,\rm init} = e_{o,\rm init}(-\sin \phi_{o,\rm init}, \cos \phi_{o,\rm init}, 0)$, where the argument of periastron $\phi_{o,\rm init}$ is uniform between 0 and 2π. The initial inner eccentricity is set to (0, 0.01, 0) for all systems.

Once the initial conditions are set, we evolve each system for 600 Myr or if one of the termination conditions is met: (1) if the planet's mass decreases below $0.03 M_j$ or its orbit becomes unbound (as a increases due to mass transfer; Equation (16)). We flag the system as being disrupted. (2) If the inner orbital period decreases below 10 days *and* the inner eccentricity is below 0.1, we then flag it as a successful migration. (3) If none of the termination flags are met at the end of the 600 Myr integration, the system is labeled as "no or partial migration." (4) We also check for orbit crossing in post-processing. If $a(1+e) >= a_o(1-e_o)$ at any moment during the evolution, we assume such systems cannot maintain long-term stability and flag them also under the disruption category.

The simulation outcome is summarized in Figure 3. In the top panel, we see that varying the phenomenological parameter A in Equation (14) effectively changes the boundary between disruption and successful migration from $\min[r_p/r_t] = 2$ to 3, covering the value of 2.7 suggested in Guillochon et al. (2011). We discuss its implication of the planetary mass loss in Section 4.1. In the bottom panel, we further show the outcome as a function of the final orbital period. As we have seen for the case studies in the previous section, high-e migration can be viewed as a two-step process, where in the first step the LK cycle periodically extracts angular momentum from the inner orbit while keeping its energy largely intact, and in the second step tidal dissipation decouples the inner planet from the outer planet and circularizes the inner orbit along a trajectory with nearly conserved orbital angular momentum. Consequently, the final semimajor axis when the orbit is circularized is about twice the minimum pericenter separation when the orbit was highly eccentric as $a(1-e^2) \simeq$ const. Notice many tidally disrupted planets do not complete the first step before disruption, and their "final" orbital periods, reported at the time of disruption, are high and approximately equal to the initial periods.

4.1. WASP-107 b Probably Did Not Lose >20% of Its Initial Mass

We explored a wide range of mass-loss efficiency due to dynamical tides by varying A between $10^{2.8}$ and 10^5 in the

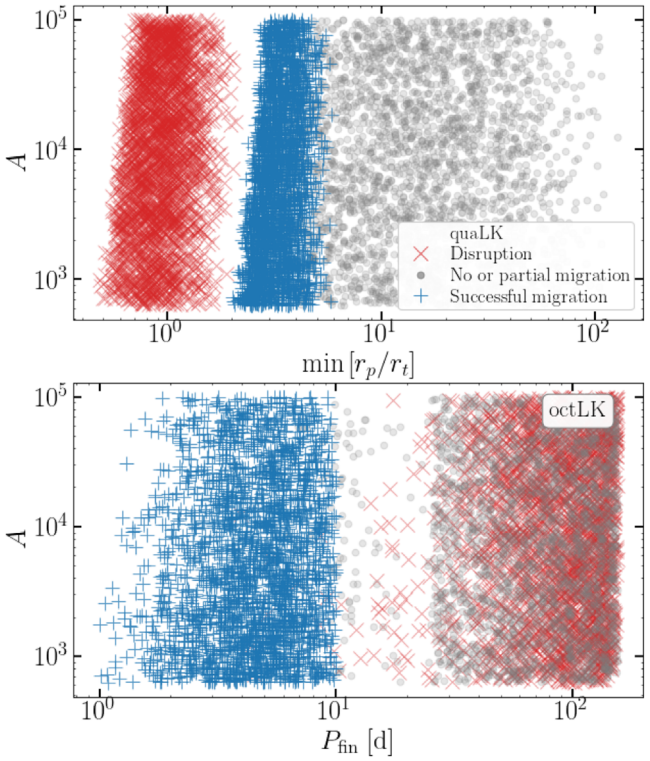

Figure 3. Population synthesis outcome over the parameter space of the phenomenological parameters A governing the mass loss (Equation (14)) as well as $\min(r_p/r_t)$ (top panel) and $P_{\rm fin}$ (bottom panel). The top panel is evolved under quaLK and the bottom panel also includes octupole interactions; yet the overall result stays the same regardless of the LK prescription. All panels assume the mass loss is nonconservative. The value of A effectively determines the boundary between disruption and survival, with increasing A shifting the critical periastron separation r_p for successful migration and the final orbital period of migrated systems both to greater values.

phenomenological mass-loss model Equation (14). However, our population synthesis suggests that WASP-107 b did not lose more than 20% of its mass during the postulated high-e migration. In other words, it did not start as a Jupiter-mass object. The reason is as follows.

Tidal interaction has a very steep dependence on the pericenter distance, and we empirically find only systems with $r_p/r_t \lesssim 3$ may experience significant mass loss. This can be understood by examining the excitation of the planetary dynamical tide (Press & Teukolsky 1977) that leads to the mass loss in Guillochon et al. (2011). The characteristic energy acquired by the dynamical tide per pericenter passage can be written as (e.g., Yu et al. 2021)

$$\frac{\Delta E_{p,\rm DT}}{E_p} \simeq 5\pi k_{2p}\left(\frac{r_t}{r_p}\right)^6 |K_{22}|^2, \tag{26}$$

where $E_p \equiv GM_p^2/R_p$. Besides the spatial overlap $\sim(r_t/r_p)^6$, there is also a temporal overlap between the prograde planetary f-mode (with spherical harmonic $l=m=2$) and the orbital drive, K_{22}, that enters the expression, and it is evaluated as (Lai 1997)

$$|K_{22}| \simeq \frac{\sqrt{2}\,z^{5/2}e^{-2z/3}}{\sqrt{15}}\left(1-\frac{\sqrt{\pi}}{4\sqrt{z}}\right), \tag{27}$$

where $z \equiv \sqrt{2}\,\omega/\Omega_{\rm peri}(\sim 10$ for systems considered in this study), with $\omega \simeq \sqrt{GM_p/R_p^3}$ is the planetary f-mode frequency (which we have approximated by the planetary dynamical frequency) and $\Omega_{\rm peri} = \sqrt{G(M_* + M_p)/r_p^3}$. The $|K_{22}|$ factor suppresses the tidal energy exponentially with increasing r_p, which, together with the work of Guillochon et al. (2011), motivates our Equation (14).[4]

On the other hand, once the mass loss is initiated, it can lead to a runaway process. The tidal radius increases as the planet loses mass because $r_t \propto M_p^{-1/3}$, whereas R_p stays nearly constant. Therefore, r_p/r_t effectively decreases after the mass loss in a previous pericenter passage. Second, a less massive inner planet is more susceptible to eccentricity excitation from the LK cycle. Both effects increase the ratio of r_p/r_t, causing a further increase in mass loss, disrupting the planet in a runaway process. The runaway is also demonstrated by the formation of a gap between the successfully migrated population and those disrupted by the host star, as shown in the top panel of Figure 3. Any planet within the gap will quickly evolve to join the disrupted population.

While changing A affects the boundary, the fractional mass loss does not sensitively depend on the value of A. Instead, we show in Figure 4 that it depends mostly on the migration time and the final orbital period, both of which further track r_p during the migration. The mass loss is limited to <20% with a smaller r_p (that is, shorter migration time and smaller $P_{\rm fin}$) leading to a greater fractional loss. The choice of quaLK or octLK does not affect the conclusion. On the other hand, a mass loss exceeding 1% requires it to be largely nonconservative. Because mass loss happens when the orbit is highly eccentric with $(1-e) \ll 1$, any conservative mass transfer exceeding 1% of the initial mass can disrupt the orbit due to the $(1-e)$ factor in the denominator in Equation (16).

The relative formation rate of WASP-107 b also depends on the mean density of the planet $\bar{\rho}_p$. As the boundary between survival and disruption is a sensitive function of r_p/r_t and $r_t \propto \rho_p^{-1/3}$, the formation rate favors planets with a high density. Empirically, the formation rate is proportional to $\lg\bar{\rho}_p$. A higher-density planet is more resistant to rapid mass loss and disruption. We thus conclude that the initial mass of WASP-107 b is likely below $0.17\,M_j$ and it lost less than 20% of its initial mass during the migration. As a caveat, however, our model does not constrain mass loss after the planet has finished high-e migration due to say photoevaporation (Spake et al. 2018, 2021; Allart et al. 2019; Kirk et al. 2020). Wang & Dai (2021) suggests that the mass-loss rate is currently low enough $1M_\oplus\,{\rm Gyr}^{-1}$ but could have been faster when the star was more active.

4.2. Initial Mutual Inclination between WASP-107 b and c

We now consider the formation outcome as a function of the initial mutual inclination between the two planets in Figure 5. A clear distinction exists when comparing quaLK (top panel) and octLK (bottom panel). In the quaLK regime, only systems with high initial mutual inclinations $I_{io,\rm init} \approx 70°$–$110°$ successfully produced a high-e migration of WASP-107 b. This is because angular momentum is the z-axis L_z is conserved in the test particle quaLK regime (Naoz 2016); thus a closer-to-perpendicular initial inclination leads to a stronger eccentricity

[4] Note, however, that we do not explicitly track the dynamical tide in our population synthesis as it is history-dependent and needs to be tracked on an orbit-by-orbit basis, which is too expensive to follow (but see Vick et al. 2019).

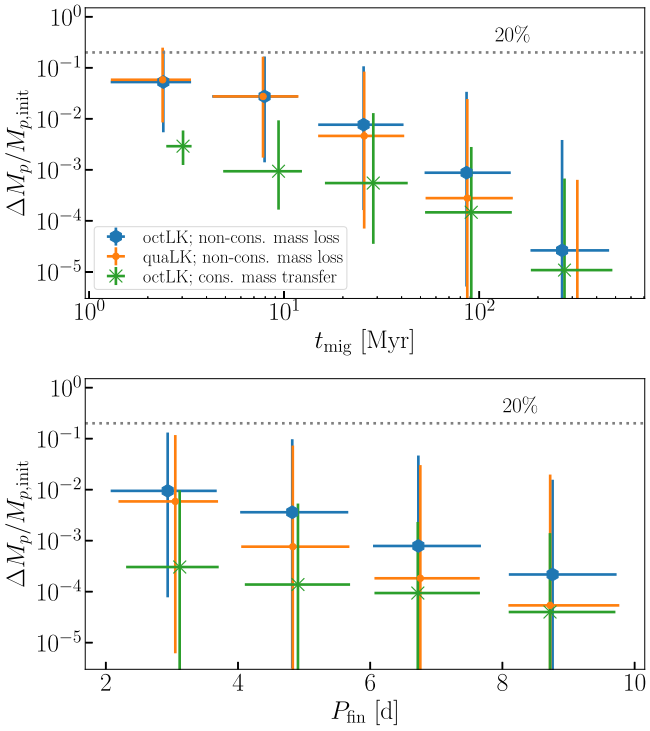

Figure 4. Fractional mass loss of successfully migrated planets as functions of the migration time (top) and the final orbital period (bottom). Error bars represent the 10th and 90th percentiles of the distribution within each bin. The planet can lose up to ∼20% of its initial mass while surviving partial disruption by the host star if the mass loss is nonconservative. A significant mass loss can happen if a system migrates with 10 s of Myr, as such a system can have small r_p/r_t during migration. The correlation between r_p and $P_{\rm fin}$ sees large scattering, so a system with $P_{\rm fin} \simeq 5$ days can still experience up to ∼10% mass loss.

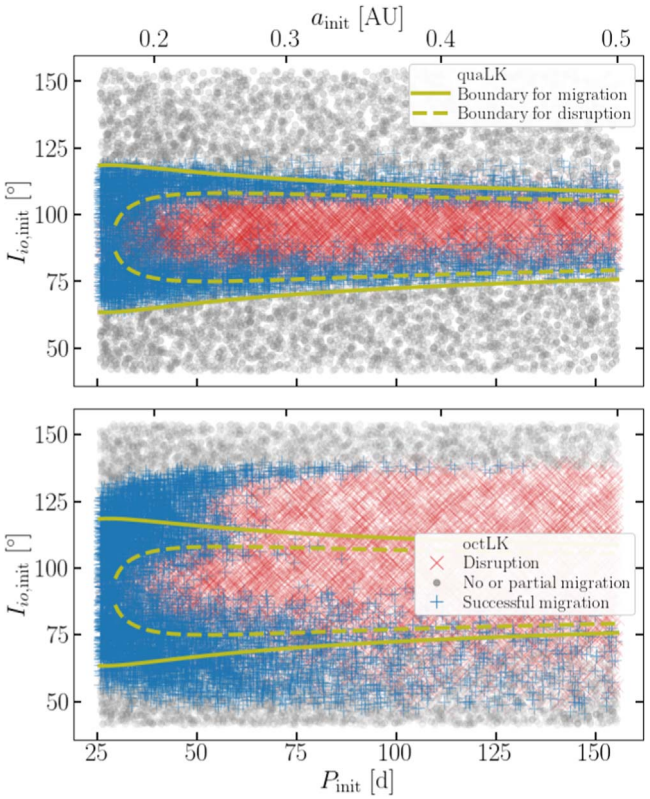

Figure 5. Outcome vs. initial inclination and period. The top panel shows systems evolved under quaLK and the bottom those under octLK. Nonconservative mass loss is assumed for both panels. For systems with $P_{\rm init} \gtrsim 75$ days, including the octupole effects make a significant difference. Under quaLK, the outcome is almost symmetric about ≃92°, and the successfully migrated systems concentrated in two narrow bands each spanning ∼10°. The analytically estimated merger window is overplotted in the solid and dashed lines. In contrast, under octLK, a prograde initial inclination is strongly favored, and both successful migration and disruption can happen over a much wider range. On the other hand, systems originating from small initial orbital periods have similar outcomes under quaLK and octLK, with the latter having a slightly wider formation window.

excitation on the inner planet. A formation window forms because the pericenter needs to be small enough to enable migration but large enough to avoid disruption (Anderson et al. 2016; Vick et al. 2019). As a reference, we also show the analytically estimated migration window between the solid and dashed lines. They are estimated using the critical values of r_p respectively given in Equations (10) and (19) with $c_{\rm dis} = 2.7$, which are further converted to the allowed range on $I_{io,\rm init}$ via Equation (11). Because of the inner orbit's backreaction on the outer one, the window is symmetric at about 92° instead of 90° (Equation (8)).

With octLK, however, significant eccentricity excitation can happen over a wider range of initial mutual inclinations (Liu et al. 2015; Petrovich 2015). WASP-107 b can be produced by high-e migration over a wider range of initial mutual inclination $I_{io,\rm init}$ ≈50°–70° between planet b and planet c. This more moderate initial mutual inclination can be produced by a less extreme dynamical process such as planet–planet scattering between planet c and/or an undetected third planet (Ford & Rasio 2008; Lu et al. 2024), or maybe a stellar flyby (Batygin et al. 2020).

4.3. WASP-107 b Most Likely Formed within the Snowline

As shown in the previous section, tidal disruption is the most likely outcome of high-e migration if the inner planet ventures too close to the host star. WASP-107 b has to have an initial orbital configuration that avoids tidal disruption. This favors a smaller initial semimajor axis for the inner planet (top panel of Figure 6). This is because at a given $I_{io,\rm init}$, a smaller initial semimajor axis provides a small lever arm for the outer planet to act on, thereby limiting the eccentricity excitation through the LK effect (see Equations (1) and (7)). In other words, the orbital eccentricity of planet b does not reach extreme values that would disrupt the planet during migration. This can also be seen by examining the merger windows in Equations (10) and (19). Note specifically that $r_{p,\rm mig} \propto a_{\rm init}^{-1/7}$, whereas $r_{p,\rm dis}$ is independent of $a_{\rm init}$. Consequently, the allowed range of r_p (hence the range of $I_{io,\rm init}$) narrows as $a_{\rm init}$ increases, which can also be seen in Figure 5. We found empirically that the relative formation rate of WASP-107 b in our population synthesis (agnostic about the prior) decreases as $\propto P_{\rm init}^{-2.4}$ (or $\propto a_{\rm init}^{-3.6}$; gray line in Figure 6). The formation rate is higher for octLK than quaLK if the initial period is less than ≈70 days as the former has a wider formation window (see later in Figure 5). For greater initial periods, octLK has a lower formation rate because more significant eccentricity excitation increases the disruption rate. If the mass loss is largely nonconservative (which is more relevant to the numerical simulations of Guillochon et al. 2011), the formation rate is 2–3 times higher than runs assuming conservative mass transfer.

As we will see later in Section 4.6, formation at large $a_{\rm init}$ is further disfavored if the tidal lag time $t_{\rm lag}$ is smaller than the

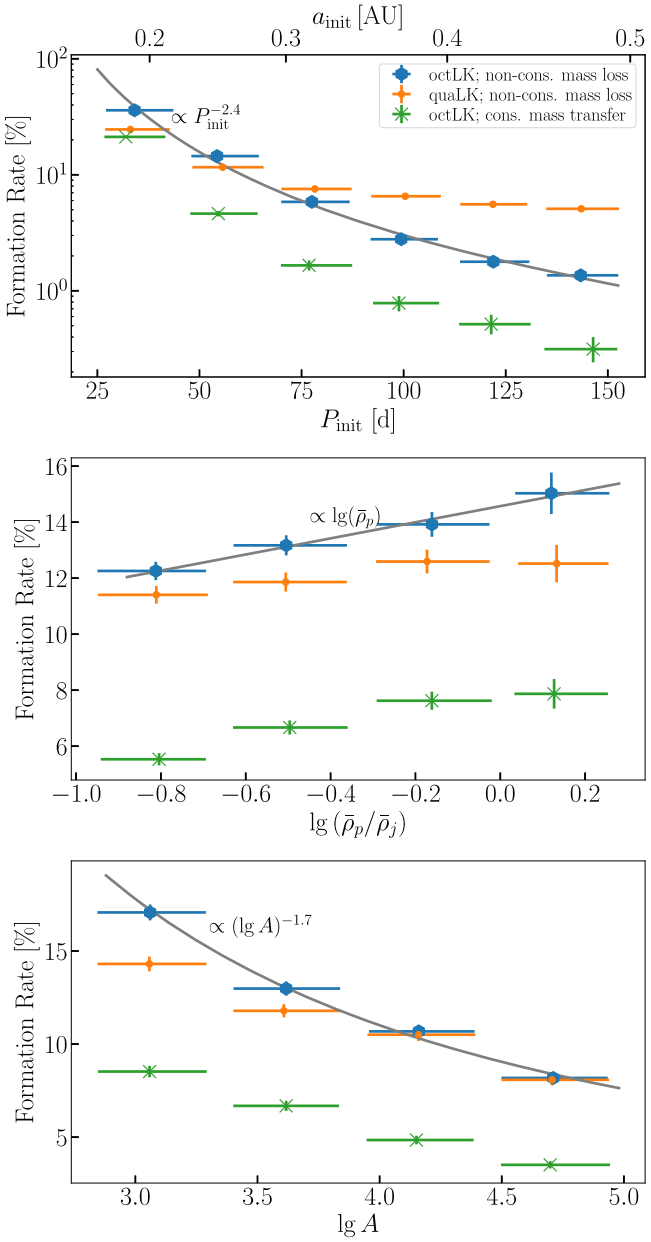

Figure 6. Formation rate of WASP-107 b–like systems as a function of the initial inner semimajor axis (top panel; also shown in the top axis is the initial orbital period), the initial planetary density (middle panel), and the phenomenological parameter lg$A$ (bottom panel). Error bars in the y-axis are the 10th and 90th percentiles assuming the number in each bin follows a Poisson distribution with the mean value given by the numerical experiment. Different colors represent different prescriptions of the synthesis (see the legend for details). Phenomenological fits to the case of octLK with nonconservative mass loss are shown in gray lines. Overall, the formation rate favors systems that experience a small amount of mass loss per orbit (small r_t and small A).

assumed $t_{\rm lag} = 10$ s. This can again be seen from Equation (10) that $r_{r,\rm mig}$ decreases with a decreasing $t_{\rm lag}$, making the allowed window narrower.

WASP-107 b most likely did not start with a semimajor axis beyond 0.5 au. This is not only due to the quickly declining relative formation rate (Figure 6) but also because a larger initial orbit for planet b would lead to an orbit crossing between planet b and planet c in our simulations. During the LK oscillation, the inner orbit will reach an eccentricity $e \simeq 1$, and the inner planet's apocenter will be at $\simeq 2a_{\rm init}$. Meanwhile, the outer orbit has an eccentricity of 0.28 today. Its value needs to be great initially because, during the LK oscillation, the outer orbit tends to extract angular momentum from the inner one. An initial inner semimajor exceeding 0.5 au will therefore cause the inner apocenter to be comparable to or greater than the outer pericenter.

The location of the snowline for a 0.6-$M_\odot$ K-star is uncertain and most likely time-dependent, but probably near or above 1 au; see Figure 1 of Kennedy & Kenyon (2008), and also (Ida & Lin 2005). This suggests that before the onset of high-e migration, WASP-107 b might have formed or migrated within the snowline. Welbanks et al. (2024) reported an atmospheric metallicity that is 10–18 × solar, and a carbon-to-oxygen ratio $\mathrm{C/O} = 0.33^{+0.06}_{-0.05}$. Sing et al. (2024) reported an even higher planetary atmospheric metallicity of 43 ± 8 times solar. The high metallicity is consistent with a low-mass progenitor for WASP-107 b when considering the mass–metallicity correlation of solar system planets and exoplanets (Welbanks et al. 2019). The low C/O ratio is also consistent with forming WASP-107 b within the water snowline (Öberg et al. 2011) as our simulations suggest. More sophisticated models that consider the locking of O into silicates also generally agree that planets that formed within the snowline should have a low C/O ratio (see, e.g., Chachan et al. 2023).

4.4. Final Inclination, Obliquity, and Orbital Period

We now compare the properties of the successfully migrated systems with the observed properties of WASP-107. In Figures 7 and 8, we show the final mutual inclination between the inner and outer planets $I_{\rm io,\ fin}$ (top panel), the stellar obliquity I_{iS} with $\cos I_{iS} = \hat{\boldsymbol{J}} \cdot \hat{\boldsymbol{S}}_*$ (middle panel), and the final orbital period of planet b $P_{\rm fin}$. Figure 7 is for systems originating from wide initial orbits, $P_{\rm init} > 75$ days, and Figure 8 is for those with 25 days $\leqslant P_{\rm init} < 40$ days.

Systems evolved under quaLK show roughly even distribution with a final mutual inclination peaking at either $I_{\rm io,\ fin} = 45°$ or 135°, insensitive to the initial orbital period. However, the distributions change significantly for octLK systems when the initial period varies. Systems that started with small periods of $P_{\rm init} < 40$ days show a distribution similar to the quaLK cases (Figure 8), whereas systems originating with $P_{\rm init} > 75$ days (top panel of Figure 7) favor a lower mutual inclination $I_{io,\rm fin} \approx 25°$–50°. If measured with Gaia astrometry (Gaia Collaboration et al. 2016; a similar measurement has been done on HAT-P-11 Xuan & Wyatt 2020), the mutual inclination can hence be used to constrain $P_{\rm init}$. An $I_{io,\rm fin} < 40°$ would suggest $P_{\rm init} > 75$ days, whereas an $I_{io,\rm fin} > 50°$ would point to an initial period $P_{\rm init} < 40$ days.

The stellar obliquity I_{iS} is shown in the middle panel of Figure 7. In both cases, the final stellar obliquity encompasses 110°, which is the empirically measured stellar obliquity (Rubenzahl et al. 2021). LK consistently launches the inner planet into a misaligned orbit around the host star thanks to the dynamical attractor effect described in Liu & Lai (2018). Similar obliquity distribution is also observed in Angelo et al. (2022) for Kepler-1656b (see, e.g., their Figure 11 for the tidally locked systems). In all cases, the orbital period distributions peak between 3 and 6 days, also consistent with the period of WASP-107 b.

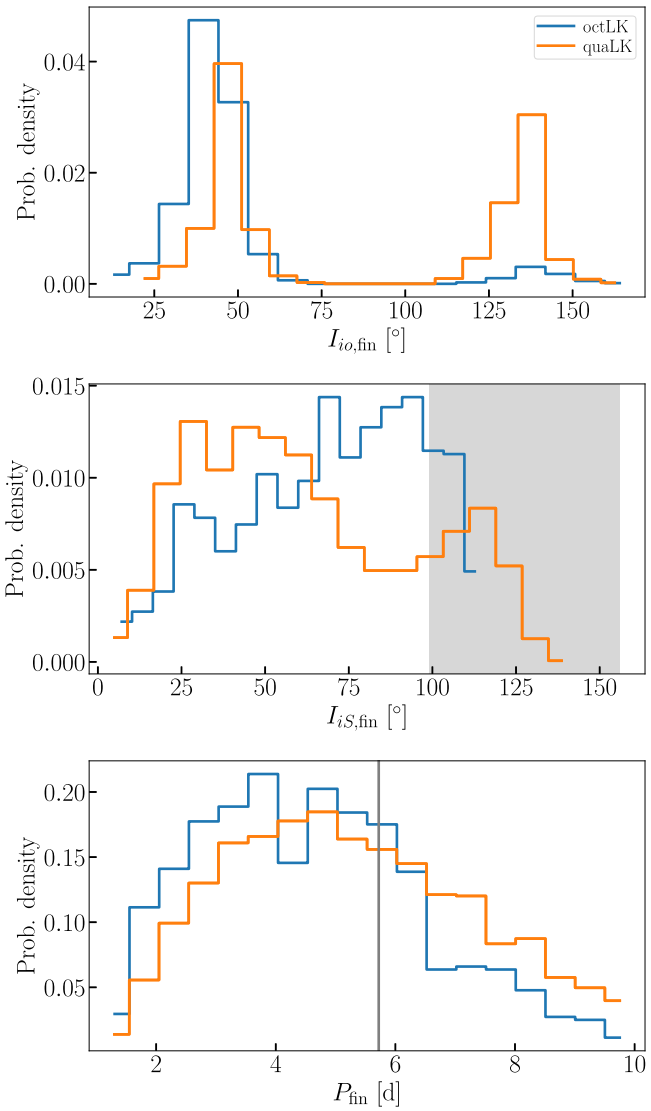

Figure 7. Distributions of the final properties for systems with initial period $P_{\mathrm{init}} > 75$ days and nonconservative mass loss. Top: mutual inclination between inner and outer orbits. A moderate mutual inclination around 25°–50° is favored under octLK. Middle: distribution of the final stellar obliquity. Both cases support a wide distribution of obliquities and are consistent with the observed near-polar configuration of WASP-107 b. This is consistent with the high inferred obliquity of WASP-107 b. The measured value (including uncertainties) is shown in the gray band. Bottom: final period. A 3–6 day final period is more favored. The gray vertical line shows the observed period (with uncertainty smaller than linewidth).

4.5. Migration Timescale

In Figure 9, the migration time, measured from the onset of LK oscillation to the point when the eccentricity drops below 0.1 and the period below 10 days, is shown as a strong function of the pericenter separation $t_{\mathrm{mig}} \propto r_p^7$. This is because $a/\dot{a}_t \propto r_p^{15/2}$ in the adopted constant time lag tidal models (Hut 1981), and a planet spends a fraction of $\sim\sqrt{1-e^2}$ of time during the LK cycle at the highly eccentric stage (Anderson et al. 2016). A secondary effect is that at a given value of $\min[r_p/r_t]$, systems evolved under octLK require longer times to migrate than those under quaLK. This is because the eccentricity oscillation under octLK is more stochastic and occasionally reaches down to a very small pericenter while the mean separation is greater.

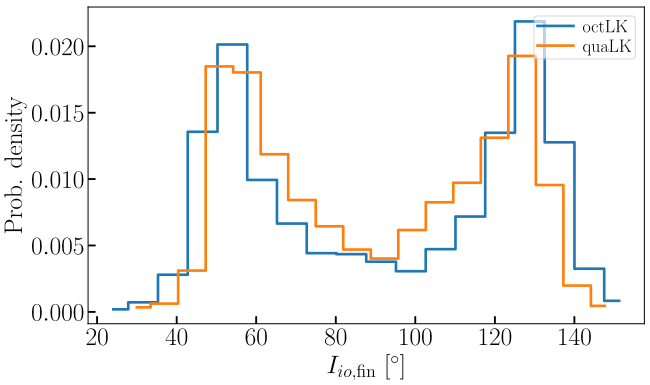

Figure 8. Similar to Figure 7 but for systems with smaller initial periods, 25 days $\leqslant P_{\mathrm{init}} < 40$ days. The octLK and quaLK simulations now show similar distributions spanning 40°–140°. The obliquity and final period distributions are similar to the quaLK results in Figure 7 and are not repeated here.

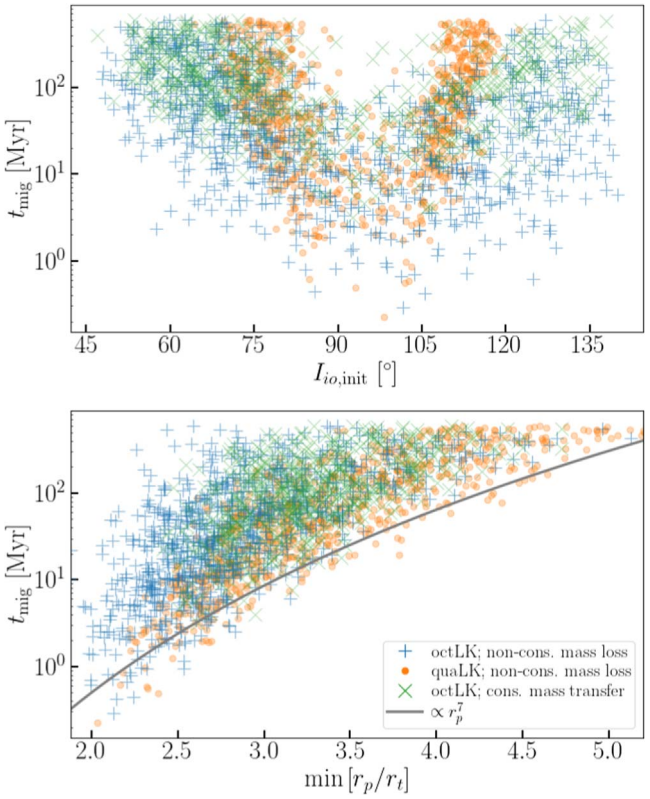

Figure 9. Migration time vs. initial inclination between inner and outer orbits (top) and the minimum pericenter separation during the LK cycle (bottom). Different colors and marker styles indicate different orders in the LK evolution and different prescriptions of mass loss/transfer (see legend).

As explained in Section 4.2, the initial mutual inclination between planets b and c often determines the minimal pericenter separation $\min[r_p/r_t]$. Therefore, the initial mutual inclination also changes the migration timescale (upper panel of Figure 9). Systems with more moderate initial mutual inclinations generate gentler, slower high-e migrations.

4.6. Impact of the Tidal Dissipation Efficiency

While we adopted $t_{\mathrm{lag}} = 10$ s as the default value for the tidal lag time, we also consider the case where $t_{\mathrm{lag}} = 1$ s for completeness. The choice of $t_{\mathrm{lag}} = 1$ s was also adopted by

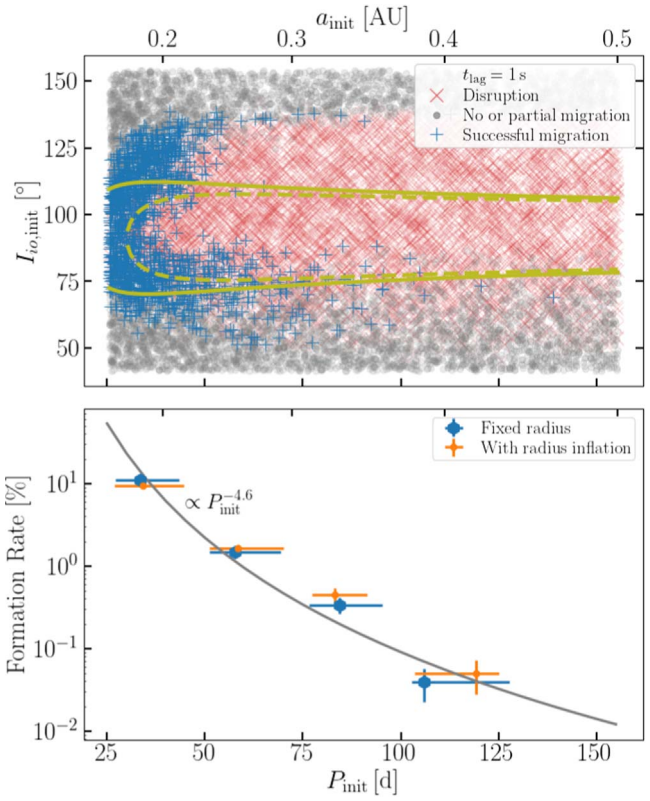

Figure 10. Formation window and rate of WASP-107-like systems with $t_{\rm lag} = 1$ s. The top panel is similar to the lower panel of Figure 5. The markers are computed for octLK systems, and the solid and dashed lines represent analytically estimated merger windows under the quadrupole approximation. The bottom panel is similar to the top panel of Figure 6. Including radius inflation or not does not change the formation window and rate significantly.

previous analyses including Anderson et al. (2016) and Vick et al. (2019). For this section, we focus on octLK with nonconservative mass loss from the planet.

The main impact of reducing $t_{\rm lag}$ from 10 s to 1 s, as illustrated in Figure 10, is that the overall formation rate is reduced by about a factor of 4. Furthermore, very few systems with $P_{\rm init} \gtrsim 100$ days can form with reduced $t_{\rm lag}$ as shown in the top panel. The formation rate also decays faster with respect to $P_{\rm init}$ as the gray line in the bottom panel depicts (see the top panel of Figure 6). This behavior can be understood by again examining the formation window determined by $r_{p,\rm dis} < r_p < r_{p,\rm mig}$. The disruption threshold (Equation (19)) is independent of both $t_{\rm lag}$ and $a_{\rm init}$, whereas the migration threshold decreases with both decreasing $t_{\rm lag}$ and increasing $a_{\rm init}$. Indeed, the analytically estimated merger window (under the quadrupole approximation) between the solid and dashed line in the top panel essentially vanishes for $P_{\rm init} \gtrsim 100$ days. Therefore, a smaller dissipation would strengthen the point we made in Section 4.3 that WASP-107 b likely started the LK oscillation within the snowline.

With $t_{\rm lag} = 1$ s, there are still systems in our simulation that experience 10%–20% radius inflation and have $L_t > 10^{-7} L_\odot$ near the end of the evolution, yet they typically have $P_{\rm fin} \lesssim 3$ days to reach the desired tidal heating rate. Similar to the case where $t_{\rm lag} = 10$ s, including the radius inflation or not affects mainly the final planetary radius but not other properties of the system, as demonstrated in the bottom panel of Figure 10. In both cases, the final obliquity ($I_{iS,\rm fin}$) and orbital inclination ($I_{io,\rm fin}$) are similar to the quaLK case shown in Figure 7, both supporting polar or even retrograde orbits.

5. Conclusions

We conclude by answering the questions we posed in the Introduction:

1. The observed WASP-107 c is indeed capable of initiating a high-e migration for WASP-107 b. The initial mutual inclination between the two planets has to be nearly orthogonal (70°–110°) in the case of quadrupole LK evolution. If including the octupole LK terms, the eccentricity excitation is more stochastic, and the initial mutual inclination can be as low as 50°, which may be more easily produced by an earlier dynamical process. Our simulations are agnostic about how the initial mutual inclination emerged. It could be planet–planet scattering (Chatterjee et al. 2008; Ford & Rasio 2008), or maybe a stellar flyby (Batygin et al. 2020). The reader is also referred to the disk-driven resonance scenario suggested by Petrovich et al. (2020). We further predict the current-day mutual inclination between the two planets to be 25°–50° should the planet originate from an initially wide orbit with a period greater than 75 days, or 40°–140° should the initial period be less than 40 days. Future Gaia observations may help to distinguish the two scenarios.
2. High-e migration can indeed explain the polar orbit of WASP-107 b (Dai & Winn 2017; Rubenzahl et al. 2021): the final stellar obliquity in our simulations encompasses 110°–120° that is reported in the literature.
3. Our simulations suggest that WASP-107 b is still circularizing and tidally decaying on its current-day 5.7 day, $e = 0.06$ orbit. With a Neptune-like tidal quality factor, the tidal heating can be as high as $10^{-6} L_\odot$, which is consistent with the observed high intrinsic temperature (Sing et al. 2024; Welbanks et al. 2024).
4. Our simulations suggest that WASP-107 b most likely started high-e migration within 0.5 au. Orbital crossing and tidal disruption are the more likely outcomes if the planet has a wider initial orbit. In other words, WASP-107 b most likely formed or migrated within the snowline before high-e migration. The observed low C/O = 0.33 (Welbanks et al. 2024) seems consistent with a formation within the water snowline.
5. Our simulations suggest that WASP-107 b most likely started with a mass no more than 20% greater than its current mass. In other words, WASP-107 b did not start as a Jupiter-mass planet. Stronger mass loss during high-e migration usually initiates a runaway tidal disruption. The fractional mass loss also strongly correlates with the migration time. If the system took 600 Myr (estimated age) to migrate, the mass loss would be minimal. 20% fractional mass loss corresponds to a fast migration of only tens of Myr.
6. WASP-107 b's radius may be only inflated during the final stage of high-e migration where both strong stellar insolation and tidal heating contributed to the inflation of the observed Jupiter-like radius.

Putting pieces together, we propose the following potential formation scenario of WASP-107 b (and planets with similar orbital architectures). The progenitor planet has an initial mass between 0.1 and 0.2 M_j (Figure 4). Before the onset of LK, it might have formed or migrated within the water snowline with a semimajor axis of <0.5 au (top panel of Figure 6). A Jupiter-like outer planet (WASP-107 c) on a moderately inclined (top

panel of Figure 9), eccentric orbit excites the inner planet to a highly eccentric orbit via octupole LK oscillations. WASP-107 b should have a smaller radius of around $0.7R_j$ before high-e migration, which helps it survive tidal disruption (middle panel of Figure 6). Yet, near the end of the LK cycle, strong tide heating may coupled with strong stellar insolation, inflating its radius to around R_j (second-last panels of Figures 1 and 2). After this inflation phase, the radius may stay inflated if the migration finished recently (less than the deflation timescale). Today, the planet is still on a misaligned, eccentric orbit. The resultant eccentricity tides cause internal heating, give a high intrinsic temperature, and partially drive the observed hydrodynamic mass loss of the planet.

During the preparation of this manuscript, Lu et al. (2024) conducted a similar analysis of the HAT-P-11 system. They performed *N*-body simulations, which can explain the initial production of a significant mutual inclination between planets b and c necessary to trigger the LK oscillation. An *N*-body simulation can also better address the stability of orbital crossing systems which we discarded in this study. On the other hand, our study allows for more flexibility in the planet's evolution (including mass loss and delayed radius evolution). A future work synthesizing the study by Lu et al. (2024) and ours will be worth investigating. Besides the mechanism discussed in this work, other mechanisms (e.g., disk-driven resonance; Petrovich et al. 2020) may also be able to explain some observed properties of WASP-107 b and similar systems. More detailed comparisons between different mechanisms at a population level should be conducted in future studies.

Acknowledgments

We thank Heather Knutson, Yayaati Chachan, Tiger Lu, Gudmundur Stefansson, and Ryan Rubenzahl for their helpful discussions. We thank Luis Welbanks, Gongjie Li, and Tiger Lu for sharing their manuscripts with us early. Computational efforts were performed on the Tempest High Performance Computing System, operated and supported by the University Information Technology Research Cyberinfrastructure at Montana State University. H.Y. acknowledges support from NSF grant No. PHY-2308415.

Data Availability

Source routines to generate results presented in this work are publicly available on GitHub at https://github.com/hangyu45/HighEccentricityMigration under a GPL-3.0 License.

ORCID iDs

Hang Yu https://orcid.org/0000-0002-6011-6190
Fei Dai https://orcid.org/0000-0002-8958-0683

References

Albrecht, S., Winn, J. N., Johnson, J. A., et al. 2012, ApJ, 757, 18
Allart, R., Bourrier, V., Lovis, C., et al. 2018, Sci, 362, 1384
Allart, R., Bourrier, V., Lovis, C., et al. 2019, A&A, 623, A58
Anderson, D. R., Collier Cameron, A., Delrez, L., et al. 2017, A&A, 604, A110
Anderson, K. R., Storch, N. I., & Lai, D. 2016, MNRAS, 456, 3671
Angelo, I., Naoz, S., Petigura, E., et al. 2022, AJ, 163, 227
Antognini, J. M. O. 2015, MNRAS, 452, 3610
Bakos, G. Á, Torres, G., Pál, A., et al. 2010, ApJ, 710, 1724
Baliunas, S. L., Donahue, R. A., Soon, W. H., et al. 1995, ApJ, 438, 269
Barker, A. J., & Ogilvie, G. I. 2009, MNRAS, 395, 2268
Batygin, K., Adams, F. C., Batygin, Y. K., & Petigura, E. A. 2020, AJ, 159, 101
Bonfils, X., Gillon, M., Udry, S., et al. 2012, A&A, 546, A27
Bouma, L. G., Palumbo, E. K., & Hillenbrand, L. A. 2023, ApJL, 947, L3
Bourrier, V., Lovis, C., Beust, H., et al. 2018, Natur, 553, 477
Butler, R. P., Vogt, S. S., Marcy, G. W., et al. 2004, ApJ, 617, 580
Chachan, Y., Knutson, H. A., Lothringer, J., & Blake, G. A. 2023, ApJ, 943, 112
Chatterjee, S., Ford, E. B., Matsumura, S., & Rasio, F. A. 2008, ApJ, 686, 580
Chen, J., & Kipping, D. 2017, ApJ, 834, 17
Curtis, J. L., Agüeros, M. A., Douglas, S. T., & Meibom, S. 2019, ApJ, 879, 49
Dai, F., & Winn, J. N. 2017, AJ, 153, 205
Dawson, R. I., & Johnson, J. A. 2018, ARA&A, 56, 175
Dyrek, A., Min, M., Decin, L., et al. 2024, Natur, 625, 51
Eggleton, P. P. 1983, ApJ, 268, 368
Ehrenreich, D., Bourrier, V., Wheatley, P. J., et al. 2015, Natur, 522, 459
Esposito, M., Covino, E., Mancini, L., et al. 2014, A&A, 564, L13
Fabrycky, D., & Tremaine, S. 2007, ApJ, 669, 1298
Ford, E. B., & Rasio, F. A. 2008, ApJ, 686, 621
Gaia Collaboration, Prusti, T., de Bruijne, J. H. J., et al. 2016, A&A, 595, A1
Gardner, J. P., Mather, J. C., Clampin, M., et al. 2006, SSRv, 123, 485
Gomes, S. R. A., & Correia, A. C. M. 2024, arXiv:2403.17896
Guillochon, J., Ramirez-Ruiz, E., & Lin, D. 2011, ApJ, 732, 74
Hartman, J. D., Bakos, G. Á, Sato, B., et al. 2011, ApJ, 726, 52
Hejazi, N., Crossfield, I. J. M., Nordlander, T., et al. 2023, ApJ, 949, 79
Hut, P. 1981, A&A, 99, 126
Ida, S., & Lin, D. N. C. 2005, ApJ, 626, 1045
Ivanov, P. B., & Papaloizou, J. C. B. 2004, MNRAS, 347, 437
Ivanov, P. B., & Papaloizou, J. C. B. 2007, MNRAS, 376, 682
Kennedy, G. M., & Kenyon, S. J. 2008, ApJ, 673, 502
Kirk, J., Alam, M. K., López-Morales, M., & Zeng, L. 2020, AJ, 159, 115
Kozai, Y. 1962, AJ, 67, 591
Kreidberg, L., Line, M. R., Thorngren, D., Morley, C. V., & Stevenson, K. B. 2018, ApJL, 858, L6
Lai, D. 1997, ApJ, 490, 847
Lampón, M., López-Puertas, M., Sanz-Forcada, J., et al. 2021, A&A, 647, A129
Lee, E. J., & Chiang, E. 2015, ApJ, 811, 41
Li, G., Naoz, S., Holman, M., & Loeb, A. 2014a, ApJ, 791, 86
Li, G., Naoz, S., Kocsis, B., & Loeb, A. 2014b, ApJ, 785, 116
Lidov, M. L. 1962, P&SS, 9, 719
Liu, B., & Lai, D. 2018, ApJ, 863, 68
Liu, B., Muñoz, D. J., & Lai, D. 2015, MNRAS, 447, 747
Lu, T., An, Q., Li, G., et al. 2024, arXiv:2405.19511
Mardling, R. A. 1995, ApJ, 450, 722
Millholland, S. 2019, ApJ, 886, 72
Naoz, S. 2016, ARA&A, 54, 441
Naoz, S., Farr, W. M., Lithwick, Y., Rasio, F. A., & Teyssandier, J. 2011, Natur, 473, 187
Naoz, S., Farr, W. M., Lithwick, Y., Rasio, F. A., & Teyssandier, J. 2013, MNRAS, 431, 2155
Naoz, S., Farr, W. M., & Rasio, F. A. 2012, ApJL, 754, L36
Öberg, K. I., Murray-Clay, R., & Bergin, E. A. 2011, ApJL, 743, L16
Paragas, K., Vissapragada, S., Knutson, H. A., et al. 2021, ApJL, 909, L10
Petrovich, C. 2015, ApJ, 799, 27
Petrovich, C., Muñoz, D. J., Kratter, K. M., & Malhotra, R. 2020, ApJL, 902, L5
Petrovich, C., & Tremaine, S. 2016, ApJ, 829, 132
Piaulet, C., Benneke, B., Rubenzahl, R. A., et al. 2021, AJ, 161, 70
Press, W. H., & Teukolsky, S. A. 1977, ApJ, 213, 183
Rubenzahl, R. A., Dai, F., Howard, A. W., et al. 2021, AJ, 161, 119
Sanchis-Ojeda, R., & Winn, J. N. 2011, ApJ, 743, 61
Sepinsky, J. F., Willems, B., Kalogera, V., & Rasio, F. A. 2007, ApJ, 667, 1170
Sing, D. K., Rustamkulov, Z., Thorngren, D. P., et al. 2024, Natur, 630, 831
Spake, J. J., Oklopčić, A., & Hillenbrand, L. A. 2021, AJ, 162, 284
Spake, J. J., Sing, D. K., Evans, T. M., et al. 2018, Natur, 557, 68
Stefànsson, G., Mahadevan, S., Petrovich, C., et al. 2022, ApJL, 931, L15
Stephan, A. P., Naoz, S., & Gaudi, B. S. 2018, AJ, 156, 128
Stephan, A. P., Naoz, S., Ghez, A. M., et al. 2016, MNRAS, 460, 3494
Stephan, A. P., Naoz, S., & Zuckerman, B. 2017, ApJL, 844, L16
Storch, N. I., Lai, D., & Anderson, K. R. 2017, MNRAS, 465, 3927
Thorngren, D. P., Fortney, J. J., Lopez, E. D., Berger, T. A., & Huber, D. 2021, ApJL, 909, L16
Tsai, S.-M., Lee, E. K. H., Powell, D., et al. 2023, Natur, 617, 483
Vick, M., & Lai, D. 2018, MNRAS, 476, 482
Vick, M., Lai, D., & Anderson, K. R. 2019, MNRAS, 484, 5645

Vick, M., Su, Y., & Lai, D. 2023, ApJL, 943, L13
von Zeipel, H. 1910, AN, 183, 345
Wang, L., & Dai, F. 2019, ApJL, 873, L1
Wang, L., & Dai, F. 2021, ApJ, 914, 99
Welbanks, L., Bell, T. J., Beatty, T. G., et al. 2024, Natur, 630, 836
Welbanks, L., Madhusudhan, N., Allard, N. F., et al. 2019, ApJL, 887, L20
Wu, Y. 2005, ApJ, 635, 688
Wu, Y. 2018, AJ, 155, 118
Xuan, J. W., & Wyatt, M. C. 2020, MNRAS, 497, 2096
Yu, H., Ma, S., Giesler, M., & Chen, Y. 2020, PhRvD, 102, 123009
Yu, H., Weinberg, N. N., & Arras, P. 2021, ApJ, 917, 31
Yu, H., Weinberg, N. N., & Arras, P. 2022, ApJ, 928, 140